Overcoming losses in superlenses with synthetic waves of complex frequency

Fuxin Guan[1]†, Xiangdong Guo[1,2]†, Kebo Zeng[1]†, Shu Zhang[2], Zhaoyu Nie[3], Shaojie Ma[1], Qing Dai[2]*, John Pendry[4]*, Xiang Zhang[1,5,6]*, Shuang Zhang[1,7]*

Superlenses made of plasmonic materials and metamaterials can image features at the subdiffraction scale. However, intrinsic losses impose a serious restriction on imaging resolution, a problem that has hindered widespread applications of superlenses. Optical waves of complex frequency that exhibit a temporally attenuating behavior have been proposed to offset the intrinsic losses in superlenses through the introduction of virtual gain, but experimental realization has been lacking because of the difficulty of imaging measurements with temporal decay. In this work, we present a multifrequency approach to constructing synthetic excitation waves of complex frequency based on measurements at real frequencies. This approach allows us to implement virtual gain experimentally and observe deep-subwavelength images. Our work offers a practical solution to overcome the intrinsic losses of plasmonic systems for imaging and sensing applications.

In conventional optical imaging, Abbe diffraction limits the resolution of feature sizes to larger than half the wavelength. This limit is due to the loss of the subwavelength information carried by evanescent waves. To overcome this limitation, a negative refractive index lens has been proposed to enhance the evanescent waves to recover the deep-subwavelength resolution of imaging (*1*, *2*). Subsequently, superlenses, made of either natural materials with negative permittivities (*3*–*7*) or hyperbolic materials with mixed signs of dielectric constants along different directions (*8*–*13*), have been proposed to attain subdiffractional limited imaging. Nevertheless, losses are non-negligible in materials with negative parameters (*14*–*16*), which reduces the deep-subwavelength information of the superlenses and seriously affects the resolution of imaging (*17*–*19*). To compensate for these losses, it has been proposed that gain materials could be incorporated into metamaterial designs or plasmonics (*20*–*27*), but the setup is extremely complicated and the gain will inevitably introduce instability and noise into the system (*28*–*30*). It has been proposed that complex-frequency waves (CFWs) with temporally growing or attenuating behaviors could provide virtual absorption or virtual gain (*31*–*35*). Some theoretical proposals have been put forward to recover the deep-subwavelength information carried by surface plasmons through the excitation of CFWs with temporal attenuation (*32*–*35*). However, synthesizing CFWs is challenging in optical systems from a practical perspective.

To address this challenge, we synthesized CFW signals using a multifrequency approach. We exploited the fact that a truncated CFW can be expressed as a combination of multiple frequency components with coefficients that follow a Lorentzian spectral lineshape through the Fourier transformation. We performed measurements at multiple real frequencies and numerically synthesized the field distribution under CFW illumination by combining the measured field plots at different frequencies according to the Lorentzian lineshape. As a proof of concept, both a SiC slab operating at optical frequencies and a bulk hyperbolic metamaterial operating at microwave frequencies were used as superlenses. We show that, although the spatial resolution of imaging at real frequencies is poor, caused by the inevitable material loss in these systems, ultrahigh resolution imaging can be obtained with synthesized CFWs that consist of multiple frequency components.

Loss compensation with CFWs

We start with an example of loss compensation for a metallic material described by the Drude model, $\varepsilon(\omega) = 1 - \omega_p/\omega + i\omega\gamma$, where γ is the nonzero ohmic loss term. Below the plasma frequency ω_p, the permittivity becomes negative, making it suitable as a plasmonic material, or for constructing hyperbolic media, to support surface or bulk waves with a very large wave vector for subdiffraction imaging. Owing to the existence of a loss term, the negative permittivity is typically accompanied by an appreciable imaginary part (left panel of Fig. 1A), which seriously limits the imaging performa Interestingly, from a mathematical perspec by transforming the frequency into the suitable complex value $\omega \rightarrow \omega - i\gamma/2$, the permittivity is turned into a purely real value $\varepsilon(\omega) = 1 - \omega_p^2/(\omega^2 + \gamma^2/4)$.

A CFW with a negative imaginary part corresponds to a wave with temporal attenuation. The mathematical expression of a CFW is expressed as $E(t) \sim e^{-i\tilde{\omega}_0 t}$, where t denotes time, $\tilde{\omega}_0 = \omega_0 - i\tau/2$, and $\tau > 0$ is the temporal attenuation factor. Although an ideal CFW exists mathematically, it is unphysical because it implies that the energy would diverge when t approaches negative infinity. Hence, a truncation at the start of time needs to be implemented to rationalize the CFW, that is, $E_T(t) = E_0 e^{-i\tilde{\omega}_0 t}\theta(t)$, where $\theta(t) = 0$ for $t < 0$ and $\theta(t) = 1$ for $t \geq 0$. Using Fourier transformation, the truncated CFW can be expanded into the integration of the spectral components $E_T(t) = \frac{E_0}{2\pi}\int \frac{1}{i(\tilde{\omega}_0 - \omega)} e^{-i\omega t} d\omega$, where the integration is from $-\infty$ to ∞ and the Fourier coefficient $1/i(\tilde{\omega}_0 - \omega)$ has a Lorentzian lineshape [for details, see supplementary materials (SM) section 6]. Hence, any response of the system at a complex frequency $\tilde{\omega}_0$, including the dielectric constant ε and the transfer function T, can be obtained via the integral of the corresponding real-frequency response, as $F(\tilde{\omega}_0) \approx \int F(\omega) \frac{1}{i(\tilde{\omega}_0 - \omega)} e^{-i\omega t + i\tilde{\omega}_0 t} d\omega/2\pi$ for sufficiently long duration t. In practice, it is sufficient to choose discrete frequency points at a certain frequency interval $\Delta\omega$ to synthesize the signal. Further, based on the compressed sensing theory (*36*–*38*), the CFW can be synthesized based on the information taken from a finite spectrum range. If the spectrum range is broad enough, the noise of the interference between different harmonics is suppressed. The system response under synthesized CFW excitation can be discretized as

$$F(\tilde{\omega}_0) \approx \sum_i F(\omega_i) \frac{1}{i(\tilde{\omega}_0 - \omega_i)} e^{-i\omega_i t + i\tilde{\omega}_0 t} \Delta\omega/2\pi \quad (1)$$

Owing to the frequency being discretized, the signal has an overall $2\pi/\Delta\omega$ temporal periodicity. Feeding the permittivity at a number of frequencies (the black and gray circles in the left panel of Fig. 1A) into Eq. 1, where F represents the permittivity, we can obtain the synthesized permittivity of complex frequency with $\tau = \gamma$, as shown in the right panel of Fig. 1A, which clearly shows that the loss of the Drude model can be largely compensated by virtual gain (for details, see SM section 7).

We use the synthetic CFW to study the imaging performance in a metal-dielectric multilayer lens with a total of 15 layers (Fig. 1B),

---

[1] New Cornerstone Science Laboratory, Department of Physics, University of Hong Kong, Hong Kong, China. [2] CAS Key Laboratory of Nanophotonic Materials and Devices, CAS Key Laboratory of Standardization and Measurement for Nanotechnology, CAS Center for Excellence in Nanoscience, National Center for Nanoscience and Technology, Beijing, China. [3] Department of Mechanical Engineering, University of California, Berkeley, CA 94720, USA. [4] The Blackett Laboratory, Department of Physics, Imperial College London, SW7 2AZ London, UK. [5] Faculty of Science, University of Hong Kong, Hong Kong, China. [6] Faculty of Engineering, University of Hong Kong, Hong Kong, China. [7] Department of Electrical and Electronic Engineering, University of Hong Kong, Hong Kong, China.

*Corresponding author. Email: daiq@nanoctr.cn (Q.D.); j.pendry@imperial.ac.uk (J.P.); xiangz@hku.hk (X.Z.); shuzhang@hku.hk (Shuang Z.)

†These authors contributed equally to this work.

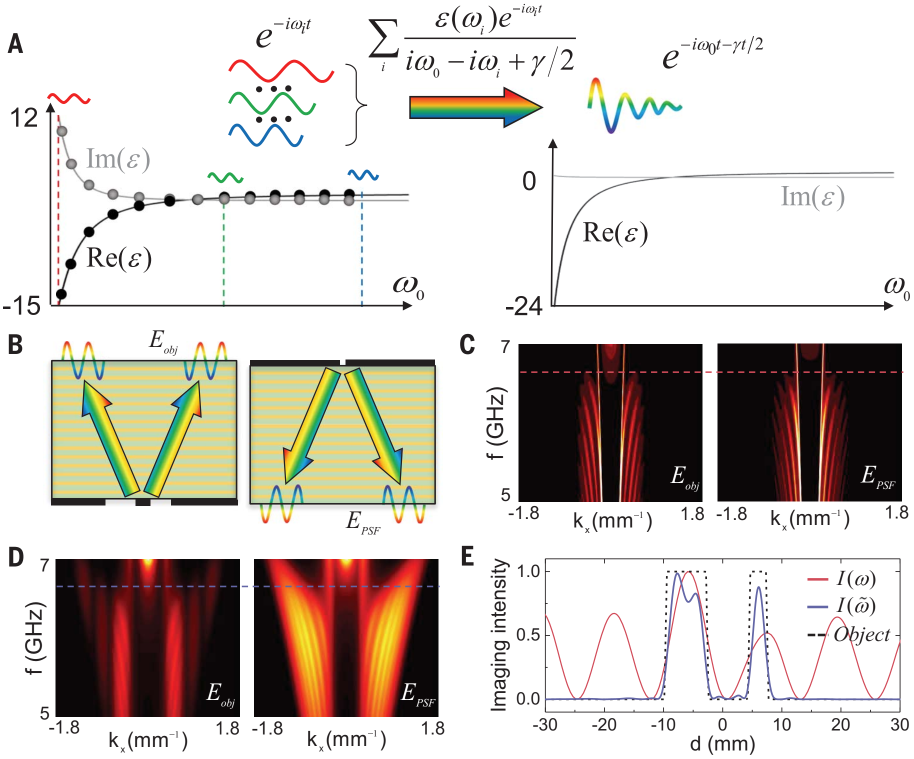

Fig. 1. Illustration of loss compensation of the superimaging lens using synthetic CFWs. (**A**) The permittivities of the Drude model with a finite damping term before (left) and after (right) loss compensation using the CFWs synthesized with permittivities at multiple frequencies. The solid circles indicate that permittivities at discretized frequencies can be used to synthesize the complex-frequency permittivity. Red, green, and blue waves and dashed lines indicate wave components at the three different frequencies and the corresponding real and imaginary parts of the permittivity. (**B**) The left panel shows a schematic of light passing through a metal-dielectric multilayer hyperbolic lens from two closely placed slits at the bottom. The thicknesses for the metal layer and the dielectric layer are d_m = 0.7 mm and d_d = 1.76 mm, respectively. The permittivity of the metal is described by the Drude model, with $\omega_p = 34\pi$ GHz and γ = 0.854 GHz. The permittivity of the dielectric medium is ε_d = 2.2. E_{obj} represents the field distribution at the top surface, whereas the right panel shows schematically the field pattern E_{PSF} generated from a point source. (**C**) The dispersion plots formed by Fourier transformation of E_{obj} and E_{PSF} at different frequencies. (**D**) The complex-frequency dispersion plots with τ = 0.854 GHz derived by synthesizing the dispersions in (C) following Eq. 1. A frequency range from 4 to 8 GHz is used to synthesize the complex-frequency results. (**E**) The corresponding imaging results at a complex frequency of (6.68 – 0.068*i*) GHz and a real frequency of 6.68 GHz, as indicated by the red and blue dashed lines in (C) and (D), respectively. *I*, intensity.

which functions as a type II hyperbolic media with mixed signs of permittivity tensor elements along different directions (*39*). The left panel of Fig. 1B schematically shows the field emitted from two closely spaced slits of different widths from the bottom of a flat hyperbolic material. The waves transmitted to the upper interface form an electric field pattern $E_{obj}(\omega, r)$, where r is the real-space coordinate. The corresponding distribution in the momentum space $E_{obj}(\omega, k)$ can be derived by Fourier transformation, where k is the in-plane wave vector. Inspired by the time-reversal imaging technique that has been demonstrated in acoustics and other wave systems (*40*–*46*), we used a postprocessing procedure to mimick a phase conjugation action to restore the image of the object. We first performed the complex conjugate operation of the momentum space distribution $E_{obj}(\omega,k)\rightarrow E^*_{obj}(\omega,k)$ and then multiplied it by the transfer function to obtain the image in the Fourier space, that is

$$E_{imag}(\omega,k) = E^*_{obj}(\omega,k)T(\omega,k) \qquad (2)$$

In this equation, the transfer function is obtained by Fourier transforming the point spread function $T(\omega,k) = \mathcal{F}[E_{PSF}(\omega,r)]$, where $E_{PSF}(\omega, r)$ is the field emitted from a point source located on one side of the hyperbolic slab to the opposite surface, as shown in the right panel of Fig. 1B. The purpose of multiplying the transfer function is to restore the original image of the object. Finally, the real-space image pattern $E_{imag}(\omega, r)$ can be obtained by the inverse Fourier transformation of Eq. 2.

We used finite element method (FEM) simulation to numerically calculate $E^*_{obj}(\omega,k)$ and $T(\omega, k)$, which are displayed in the left and right panels of Fig. 1C, respectively. The calculated image pattern based on Eq. 2 at frequency f = 6.68 GHz is shown by the red line in Fig. 1E, which deviates from the object (shown as the dashed line). By contrast, by performing phase conjugation in the complex-frequency domain (*47*, *48*), that is, by constructing the $E^*_{obj}(\tilde{\omega},k)$ and $T(\tilde{\omega},k)$, respectively, using Eq. 1 with $\tau = \gamma$, the large wave vector components are recovered (Fig. 1D). The complex-frequency image faithfully follows the original pattern, as shown by the blue line in Fig. 1E, verifying the capability of the multifrequency approach to synthesize the CFW for substantially enhancing the imaging resolution compared with that of the real frequency (red line in Fig. 1E).

Experimental results

Microwaves

Equations 1 and 2 require the distribution of both amplitude and phase of field, which can be readily obtained using a microwave characterization setup for a flat hyperbolic metamaterial lens designed to operate at microwave frequencies. The unit cell of the metamaterial consists of a spiral metallic wire–dielectric layer with the dimensions 4 mm by 4 mm by 1.5 mm to form a type II hyperbolic metamaterial with two identical in-plane negative permittivities and one out-plane positive permittivity, as shown in Fig. 2A. The spiral structure can reduce the plasma frequency such that the accessible wave vectors in the Brillouin zone can be much larger than those in the free space. The corresponding equifrequency contours (EFCs) at different frequencies are retrieved using full-wave simulations, as shown in Fig. 2B, where the frequencies of the EFCs increase along the direction of the arrow. At higher frequencies and in the absence of loss, the EFC can reach the horizontal Brillouin edge, providing large in-plane wave vectors for achieving subdiffractional imaging resolution. The corresponding in-plane EFCs are depicted in fig. S3. Figure 2C displays the experimental setup, wherein the bulk metamaterial lens is composed of 80-by-80 in-plane unit cells and 25 layers vertically. A dipole source is placed at the bottom of the sample, and a probe antenna is raster scanned at the top surface to measure the near-field distribution. The details of the experimental setup and samples are depicted in SM sections 1 to 3.

To begin, we scanned a one-dimensional (1D) line above the sample to measure the field distribution, as depicted in Fig. 2D, emitted from a single dipole source across 251 discrete frequency points within the range of 5 to 7.5 GHz. The dispersion is subsequently obtained by Fourier transformation (Fig. 2E). The dispersion plot exhibits two bright lines in the middle, which locate near the light cone in the dielectric material, whereas the other bright lines

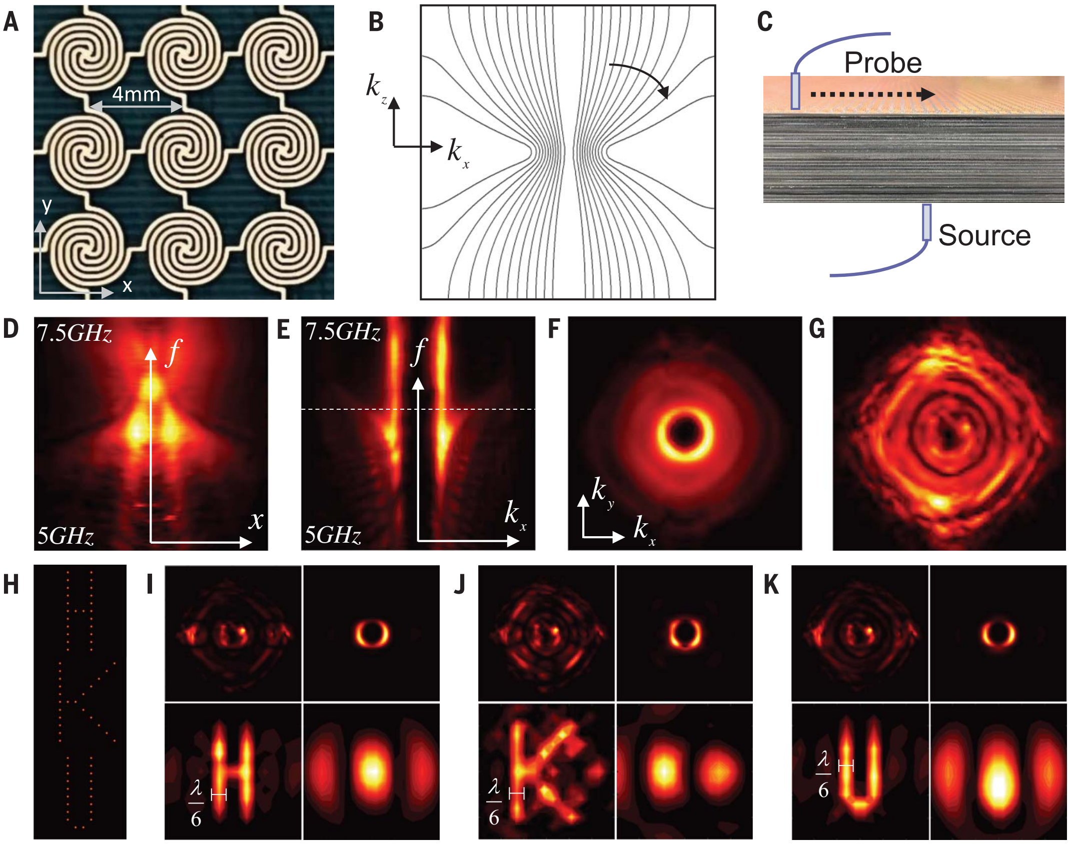

Fig. 2. Experimental demonstration of loss compensation in superimaging using a hyperbolic lens at microwave frequency. (**A** and **B**) Photograph of hyperbolic metamaterial with metallic spiral wires of 0.2-mm width printed on a 1.5-mm-thick Teflon slab (A). The EFCs in the Brillouin zone at different frequencies are depicted in (B), with the frequencies distributed evenly between 0.9 and 6.5 GHz. The Brillouin zone boundaries along the vertical and horizontal directions are π/(4 mm) and π/(1.5 mm), respectively. The arrow implies the direction of increased frequency of the EFCs. (**C**) Schematic of the experimental setup with the two dipole antennas placed near the top and bottom interfaces of the sample, with the bottom and top antennas serving as source and probe, respectively. (**D**) The measured electric field distribution along a line from –150 to +150 mm at the top interface with a frequency step of 0.01 GHz, which locates in the same *y-z* plane as the source antenna. (**E**) The dispersion plot obtained by spatial Fourier transformation of the field distribution shown in (D). (**F**) The 2D electric field distribution in the momentum space at a frequency of 6.5 GHz, which serves as the transfer function. (**G**) The 2D electric field distribution in the momentum space for a CFW with a frequency of (6.5 – 0.0065*i*) GHz synthesized by the measurements at multiple frequencies. (**H**) The ground truth of the letters H, K, and U. (**I** to **K**) The imaging results with the dipole sources arranged in the shape of the three letters. The top and bottom subpanels correspond to the Fourier space field distributions and real-space intensity distributions, and the left and right subpanels show the complex-frequency and real-frequency results, respectively.

with larger wave vectors correspond to the hyperbolic modes. Limited by the damping of the system, the measured Fourier components in the momentum space are far from reaching the Brillouin zone edge. Because the frequency marked by the white dashed line (f = 6.5 GHz) exhibits relatively large wave vectors, it is selected as the central frequency for the signal synthesis. The 2D field distribution in the momentum space at the central frequency is shown in Fig. 2F, and the distributions at a number of other frequencies are provided in SM section 8. Using Eq. 1, we synthesized the dispersion of the complex frequency using 251 frequency points, with the temporal snapshot captured at the end of the temporal periodicity (Fig. 2G). Notably, the synthesized results with complex-frequency excitation recover the field components across a large portion of the Brillouin zone, indicating a much better spatial resolution than that of the real frequency. Note that the Fourier space distributions shown in Fig. 2, F and G, correspond to the $T(\omega, k)$ and $T(\tilde{\omega}, k)$ of the real-frequency and complex-frequency cases in Eq. 2, respectively.

We next showcase super-resolution imaging of subwavelength patterns with the synthesized complex frequency. The desired pattern is formed by sequentially placing a single emitting dipole antenna at different locations, and the field distribution at the top surface is measured at each location of the dipole source. The measured field distributions are then linearly superimposed to form the image. Subsequently, Fourier transformation is performed to obtain the Fourier pattern at the real and complex frequencies, $E^*_{\mathrm{obj}}(\omega, k)$ and $E^*_{\mathrm{obj}}(\tilde{\omega}, k)$. The ground truth of three different patterns, letters H, K, and U, are shown in Fig. 2H, and the corresponding imaging results obtained by using Eq. 2 are displayed in Fig. 2, I to K, respectively. The top-left image in each subpanel shows the Fourier pattern with synthesized complex-frequency excitation, which occupies a substantial portion of the Brillouin zone, whereas the corresponding bottom-left image of each subpanel displays the image of the subwavelength letters. By contrast, the imaging results at the real frequency are shown in the right subpanels for all three cases, and, in each case, the original pattern cannot be identified, thereby confirming a substantial improvement in superimaging with the complex-frequency approach, from λ/2 to λ/6, where λ is the free-space wavelength at the central frequency (6.5 GHz) of the synthesized CFW.

We next investigated the effect of the number of frequency points used to synthesize the complex-frequency response on the superimaging

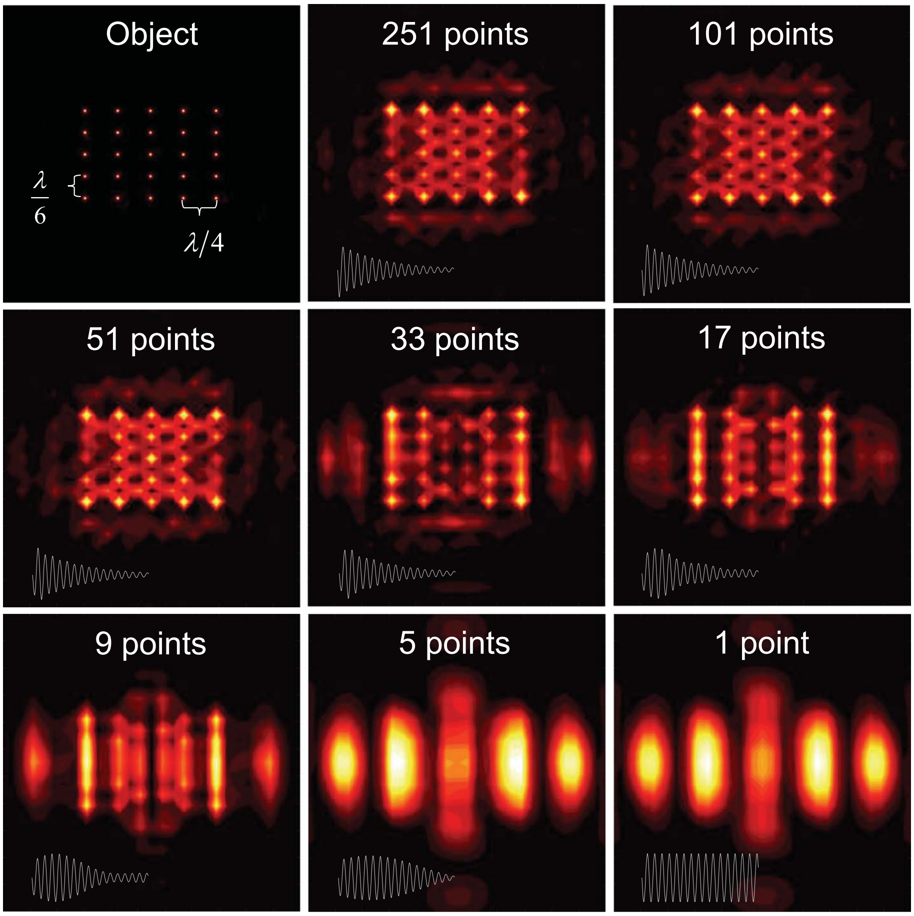

Fig. 3. Investigation of the dependence of the imaging quality over the number of frequency points. The ground truth is shown in the top-left panel, which consists of a five-by-five antenna array, where the lattice constants along the *x* and *y* directions are λ/4 and λ/6, respectively. The other panels show the image intensity distributions that were obtained using different numbers of frequency points, with the central frequency fixed at 6.5 GHz and a fixed frequency step of 0.01 GHz. The corresponding synthetic temporal signal is depicted in the inset of each panel.

performance, with the results shown in Fig. 3. The top-left subpanel of the figure displays the object, which is composed of a five-by-five array of dipole antennas. The horizontal and vertical lattice constants are one-fourth and one-sixth of the central wavelength, respectively. We gradually reduced the number of frequency points from 251 to 1 to construct the synthetic imaging patterns, with a fixed frequency step of 0.01 GHz, and the corresponding synthesized temporal signals are depicted in the insets. Our study shows that reducing the number of frequency points to 51 has a negligible impact on image quality. However, as we continued to reduce the number of frequency points, there was a substantial decrease in imaging resolution, causing the images of the dipoles to merge into vertical lines. When the number of frequency points drops below 17, these lines become wider in the horizontal direction. The corresponding Fourier distributions are shown in fig. S6. This highlights the importance of having a sufficient number of frequency points to maintain good spatial resolution and avoid image degradation.

Infrared

To showcase the versatility of the complex-frequency method, we used a silicon carbide (SiC) superlens operating at mid-infrared (mid-IR) frequency to investigate the loss compensation for superimaging. The design of the superlens is based on a SiC sandwich structure (Fig. 4A), in which the upper and lower surfaces correspond to the image and object planes of the lens, respectively (*6*). The fabrication technique can be found in SM sections 4 and 5. The object is composed of a 1D grating of varying spacings or circular apertures of varying diameters patterned on a metal film [scanning electron microscopy (SEM) image shown in the inset of Fig. 4B]. The optical image is captured by the technique of scattering-type scanning near-field optical microscopy (s-SNOM). With this technique, both the amplitude and phase of the image field can be collected by the probe. The measured field pattern of the 1D grating at the image plane is Fourier analyzed at different frequencies and presented in Fig. 4B. Here, the frequency interval is 2 cm^{-1}, from 900 to 980 cm^{-1}, with a total of 41 points. Figure 4C displays the profiles of the grating captured by the SiC superlens at both the complex and real frequencies, in both real space (left panel) and momentum space (right panel). These profiles demonstrate superior imaging quality at the complex frequency compared with the real frequency.

The SEM image of the array of 2D circular apertures is shown in Fig. 4D. The field distributions in Fig. 4, E to G, correspond to the images captured at the complex frequency and two distinct real frequencies, respectively. The complex-frequency image closely resembles the SEM image, whereas only heavily blurred field patterns are observed at the real frequencies. To investigate the resolution limitations of the SiC superlens with loss compensation, two pairs of holes placed closely together, but with varying displacements, were fabricated; Helium ion microscopy (HIM) images are shown in Fig. 4H. The corresponding s-SNOM images at the complex and real frequencies are shown in Fig. 4, I and J, respectively. Using the complex-frequency method, two pairs of circles with edge-to-edge separations of 40 and 100 nm, respectively, can be clearly resolved, whereas no discernible images are formed at the real frequency. The spatial resolution shown in the measurement of the double-aperture structure using complex frequency is around 400 nm, as shown in Fig. 4I, whereas the distance between two neighboring field maxima at the corresponding central frequency is around 1200 nm, as shown in Fig. 4G.

Concluding remarks

We have presented a method to compensate for the intrinsic loss of hyperbolic metamaterial and for SiC superimaging lenses by synthesizing a complex-frequency excitation through a multifrequency approach, which improves imaging resolution beyond the limit imposed by the damping of the system. Our approach successfully overcomes the challenges of experimentally implementing CFWs in the time domain, which include the need for precise CFW synthesis and time-gated measurements after reaching the quasi–steady state, and holds great potential for high-resolution microscopy. Furthermore, the synthesized complex-frequency approach can be extended to other areas of optics, such as plasmonic sensing applications. By leveraging the enhanced quality factor of plasmonic structures, our approach has the potential to substantially improve sensitivity in sensing applications. In addition, the approach can be tailored to different systems and geometries, providing a flexible and versatile tool for improving optical performance.

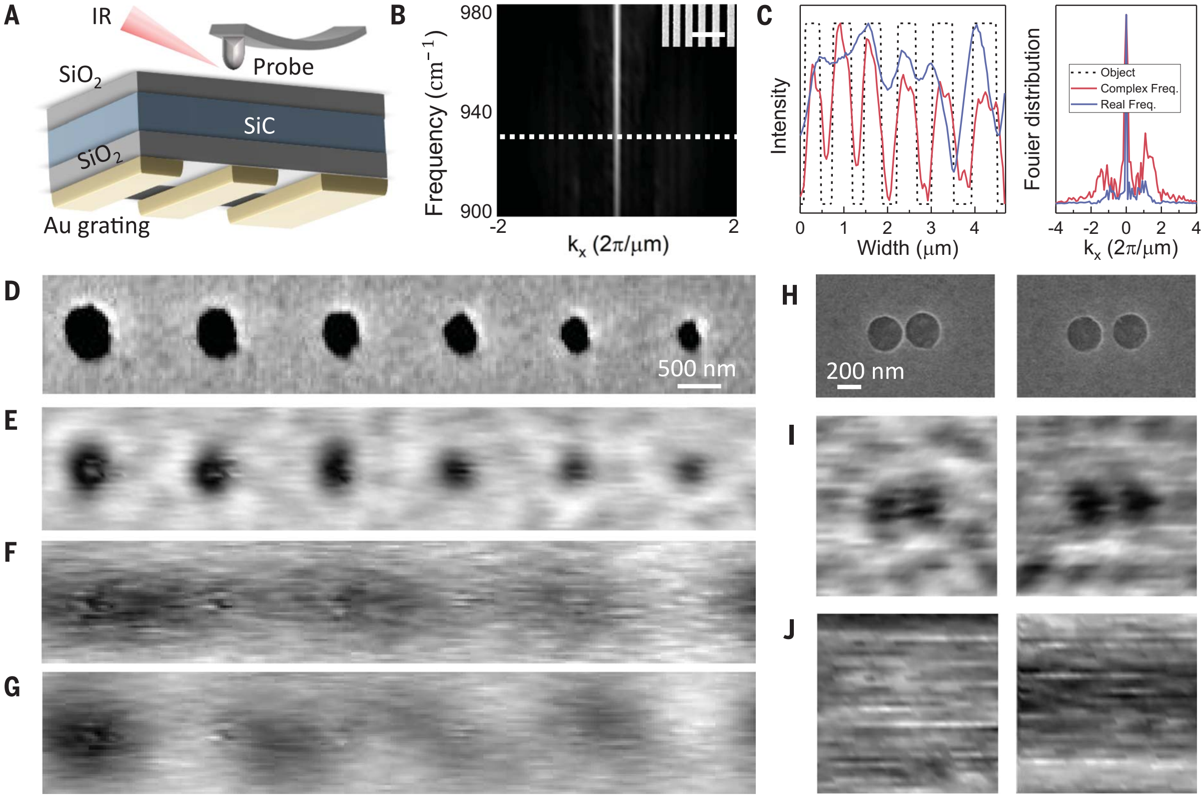

Fig. 4. Experimental observation of loss compensation in mid-IR superimaging using a SiC superlens. (**A**) Schematic of the s-SNOM experimental setup. A ~440-nm-thick SiC layer is sandwiched between two SiO$_2$ layers of equal thickness (~220 nm). A 60-nm-thick gold grating is placed at the bottom. (**B**) Fourier distribution of a line scan at the imaging plane in the 1D grating structure with varying spacings (SEM image is shown in the inset; scale bar, 2 μm). The dashed line represents the central frequency of 930 cm^{-1}. (**C**) Imaging patterns at both the complex frequency $\tilde{f} = (930 - 12i)$ cm^{-1} and real frequency of 930 cm^{-1}, in both the real space (left) and momentum space (right). (**D**) SEM image of a thin gold film with an array of holes of different diameters. (**E**) Image of the electric field at the complex frequency $\tilde{f}$. (**F** and **G**) Real-frequency images at 922 cm^{-1} (F) and 930 cm^{-1} (G). (**H**) HIM images of pairs of circular holes with different spatial separations. (**I** and **J**) Images correspond to electric field distributions of the images at the complex frequency $\tilde{f}$ = (930 – 12i) cm^{-1} (I) and real frequency of 930 cm^{-1} (J).

REFERENCES AND NOTES

1. V. G. Veselago, *Sov. Phys. Usp.* **10**, 509–514 (1968).
2. J. B. Pendry, *Phys. Rev. Lett.* **85**, 3966–3969 (2000).
3. N. Fang, H. Lee, C. Sun, X. Zhang, *Science* **308**, 534–537 (2005).
4. D. Melville, R. Blaikie, *Opt. Express* **13**, 2127–2134 (2005).
5. X. Zhang, Z. Liu, *Nat. Mater.* **7**, 435–441 (2008).
6. T. Taubner, D. Korobkin, Y. Urzhumov, G. Shvets, R. Hillenbrand, *Science* **313**, 1595 (2006).
7. T. Li *et al.*, *Photonics Insights* **2**, R01 (2023).
8. Z. Liu, H. Lee, Y. Xiong, C. Sun, X. Zhang, *Science* **315**, 1686 (2007).
9. I. I. Smolyaninov, Y. J. Hung, C. C. Davis, *Science* **315**, 1699–1701 (2007).
10. S. Dai *et al.*, *Nat. Commun.* **6**, 6963 (2015).
11. P. Li *et al.*, *Nat. Commun.* **6**, 7507 (2015).
12. P. A. Belov, C. R. Simovski, P. Ikonen, *Phys. Rev. B* **71**, 193105 (2005).
13. P. A. Belov *et al.*, *Phys. Rev. B* **77**, 193108 (2008).
14. L. D. Landau, E. M. Lifshitz, L.P. Pitaevskii, *Electrodynamics of Continuous Media*, vol. 8 of *Landau and Lifshitz Course of Theoretical Physics* (Pergamon Press, 1984).
15. M. I. Stockman, *Phys. Rev. Lett.* **98**, 177404 (2007).
16. P. Kinsler, M. W. McCall, *Phys. Rev. Lett.* **101**, 167401 (2008).
17. D. R. Smith *et al.*, *Appl. Phys. Lett.* **82**, 1506–1508 (2003).
18. R. Merlin, *Appl. Phys. Lett.* **84**, 1290–1292 (2004).
19. I. A. Larkin, M. I. Stockman, *Nano Lett.* **5**, 339–343 (2005).
20. S. Anantha Ramakrishna, J. B. Pendry, *Phys. Rev. B* **67**, 201101 (2003).
21. A. Fang, T. Koschny, M. Wegener, C. M. Soukoulis, *Phys. Rev. B* **79**, 241104 (2009).
22. S. Xiao *et al.*, *Nature* **466**, 735–738 (2010).
23. A. Fang, T. Koschny, C. M. Soukoulis, *Phys. Rev. B* **82**, 28–31 (2010).
24. J. M. Hamm, S. Wuestner, K. L. Tsakmakidis, O. Hess, *Phys. Rev. Lett.* **107**, 167405 (2011).
25. J. Grgić *et al.*, *Phys. Rev. Lett.* **108**, 183903 (2012).
26. R. S. Savelev *et al.*, *Phys. Rev. B* **87**, 115139 (2013).
27. M. Sadatgol, Ş. K. Özdemir, L. Yang, D. O. Güney, *Phys. Rev. Lett.* **115**, 035502 (2015).
28. M. I. Stockman, *Phys. Rev. Lett.* **106**, 156802 (2011).
29. S. Wuestner, A. Pusch, K. L. Tsakmakidis, J. M. Hamm, O. Hess, *Phys. Rev. Lett.* **107**, 259701 (2011).
30. J. B. Pendry, S. A. Maier, *Phys. Rev. Lett.* **107**, 259703 (2011).
31. H. Li, A. Mekawy, A. Krasnok, A. Alù, *Phys. Rev. Lett.* **124**, 193901 (2020).
32. A. Archambault, M. Besbes, J. J. Greffet, *Phys. Rev. Lett.* **109**, 097405 (2012).
33. K. L. Tsakmakidis, T. W. Pickering, J. M. Hamm, A. F. Page, O. Hess, *Phys. Rev. Lett.* **112**, 167401 (2014).
34. H. S. Tetikol, M. I. Aksun, *Plasmonics* **15**, 2137–2146 (2020).
35. K. L. Tsakmakidis, K. G. Baskourelos, M. S. Wartak, *Metamaterials and Nanophotonics: Principles, Techniques and Applications* (World Scientific, 2022).
36. D. L. Donoho, M. Vetterli, R. A. DeVore, I. Daubechies, *IEEE Trans. Inf. Theory* **44**, 2435–2476 (1998).
37. D. L. Donoho, *IEEE Trans. Inf. Theory* **52**, 1289–1306 (2006).
38. P. Zheng *et al.*, *Adv. Opt. Mater.* **10**, 2200257 (2022).
39. D. R. Smith, J. B. Pendry, *J. Opt. Soc. Am. B* **23**, 391 (2006).
40. D. R. Jackson, D. R. Dowling, *J. Acoust. Soc. Am.* **89**, 171–181 (1991).
41. D. Cassereau, M. Fink, *IEEE Trans. Ultrason. Ferroelectr. Freq. Control* **39**, 579–592 (1992).
42. C. Draeger, M. Fink, *Phys. Rev. Lett.* **79**, 407–410 (1997).
43. J. de Rosny, M. Fink, *Phys. Rev. Lett.* **89**, 124301 (2002).
44. G. Lerosey *et al.*, *Phys. Rev. Lett.* **92**, 193904 (2004).
45. S. Maslovski, S. Tretyakov, *J. Appl. Phys.* **94**, 4241–4243 (2003).
46. J. B. Pendry, *Science* **322**, 71–73 (2008).
47. T. Zhu, *Geophys. J. Int.* **197**, 483–494 (2014).
48. K. Wapenaar, J. Brackenhoff, J. Thorbecke, in vol. 1 of *81st EAGE Conference and Exhibition* (European Association of Geoscientists and Engineers, 2019), pp. 2572–2576.

ACKNOWLEDGMENTS

Funding: This work was supported by the New Cornerstone Science Foundation, the Research Grants Council of Hong Kong (AoE/P-502/20 and 17309021), the National Natural Science Foundation of China (51925203 and 52102160), and the Strategic Priority Research Program of the Chinese Academy of Sciences (grant no. XDB36000000). **Author contributions:** Shuang Z. and X.Z. conceived the project. Shuang Z. and F.G. proposed using measurements at multiple real frequencies to obtain a complex-frequency measurement. F.G. and K.Z. performed numerical simulations and analytical calculations under the guidance of Shuang Z. F.G. carried out the microwave experiment. X.G., Shu Z., and Q.D. carried out the s-SNOM experiment. F.G., X.G., K.Z., Z.N., S.M., Q.D., J.P., X.Z., and Shuang Z. participated in the analysis of the results. F.G., X.G., and Shuang Z. wrote the manuscript with input from all authors. All authors contributed to the discussion. **Competing interests:** The authors declare no conflicts of interest. **Data and materials availability:** All data are available in the main text or the supplementary materials.

SUPPLEMENTARY MATERIALS

science.org/doi/10.1126/science.adi1267
Materials and Methods
Supplementary Text
Figs. S1 to S8
References

Submitted 5 April 2023; accepted 29 June 2023
10.1126/science.adi1267